

## Article

# Enhancing Transient Response and Voltage Stability of Renewable Integrated Microgrids

Luay Elkhidir <sup>1</sup>, Khalid Khan <sup>1</sup> , Mohammad Al-Muhaini <sup>1,2</sup>  and Muhammad Khalid <sup>1,2,3,\*</sup> 

<sup>1</sup> Electrical Engineering Department, King Fahd University of Petroleum and Minerals (KFUPM), Dhahran 31261, Saudi Arabia; g201707630@kfupm.edu.sa (L.E.); g201604320@kfupm.edu.sa (K.K.); muhaini@kfupm.edu.sa (M.A.-M.)

<sup>2</sup> Center for Renewable Energy and Power Systems, KFUPM, Dhahran 31261, Saudi Arabia

<sup>3</sup> K.A. CARE Energy Research & Innovation Center, Dhahran 31261, Saudi Arabia

\* Correspondence: mkhalid@kfupm.edu.sa

**Abstract:** Integration of renewable generation coupled with an energy storage system (ESS) in a power system increases the complexity of networks' stability analysis and control. Therefore, an accurate stability assessment of power networks is expected to become a big challenge in the future. In this work, an effective approach to prevent power outage by controlling the source voltage of the power network is formulated to mitigate the effects of grid faults. Small signal stability studies are conducted on a renewable integrated IEEE 9 bus system as a case study with optimized size and allocation of ESS for reducing output power variability of renewables. An assessment is performed to study the effects of load-sharing devices on parallel generators under 6-cycle three-phase fault disturbances. The damping of the power network is increased at nominal and light loading conditions with 6-cycle three-phase fault disturbances through coordinated power system stabilizer (PSS) and static VAR compensator (SVC) at bus 9. The developed framework is extensively analyzed in steady-state conditions using a load flow program. Based on the results obtained, the proposed coordinated PSS-SVC device proves to possess comparatively better performance in terms of enhancing most of the system response rate under various load conditions with overall improved stability.

**Keywords:** grid fault restoration; renewable microgrid; power system stabilizer; voltage stability



**Citation:** Elkhidir, L.; Khan, K.; Al-Muhaini, M.; Khalid, M. Enhancing Transient Response and Voltage Stability of Renewable Integrated Microgrids. *Sustainability* **2022**, *14*, 3710. <https://doi.org/10.3390/su14073710>

Academic Editor: Pablo García Triviño

Received: 27 January 2022

Accepted: 9 March 2022

Published: 22 March 2022

**Publisher's Note:** MDPI stays neutral with regard to jurisdictional claims in published maps and institutional affiliations.



**Copyright:** © 2022 by the authors. Licensee MDPI, Basel, Switzerland. This article is an open access article distributed under the terms and conditions of the Creative Commons Attribution (CC BY) license (<https://creativecommons.org/licenses/by/4.0/>).

## 1. Introduction

Today, power system grids are more complicated and expansive, as electricity plays an important role in almost all aspects of humankind. Therefore, it is pertinent to mitigate the blackout probability and its period to increase the level of security and welfare. Small signal stability is defined as “the ability of a power system to maintain synchronism under small disturbance”. The impact of power quality appears in dynamic system and electric power industry which can be significantly expensive [1]. Power quality is usually defined as the ability of the power system networks to transfer a stable, uninterrupted, and clean power supply with a pure noise-free sinusoidal waveform. Power system plants are frequently exposed and sustain disturbances as they are non-linear dynamic systems. These disturbances may lead to partial or blackout, which can produce severe consequences [2].

Nowadays, parallel standby power systems are used instead of single large generator units. These backup power systems play an increasingly significant role in ensuring an uninterrupted supply of power. Parallel operation of generator sets (parallel power systems) provides many benefits such as reliability, expandability, flexibility, ease of maintenance, and quality performance. Generally, the load shedding technique is investigated under these operations [3,4]. Decades ago, the series capacitive compensation technique was used for reactive power control and damping out the oscillations to improve the transmitted power [5,6]. Then the use of automatic controls like power system stabilizers (PSSs) in large power systems grids became essential to maintain stability. The power system stabilizer is

used to provide supplementary feedback stabilizing control signals to the excitation system for mitigating the electro-mechanical oscillations [7].

The concept of microgrid formulation facilitates exclusive control over selected intensive problems associated with renewable integration [8–10]. Typically, a microgrid includes control theory to sustain a distributed generator, energy storage system, and local loads. The microgrid can be operated in an islanded as well as grid-connected mode [11]. This allows the formation of a deregulated power network that is pertinent considering the complexities of renewable integration. Hence, microgrid helps to increase renewable penetration in the energy sector with enhanced control over the grid elements maintaining the reliability and security of the supplied power [12–14]. Accordingly, further development in power electronics has led to the large-scale incorporation of flexible AC transmission system (FACTS) devices in electrical power plants [15]. This technique is one type of variable series compensation which is very effective for enhancing stability as well as controlling power flow in the transmission lines. The occurrence of electrical disturbances like faults and lightning are damped out by incorporation of static VAR compensator (SVC) in combination with PSS and automatic voltage regulators (AVR) in large power systems [16].

A variety of energy sources with different characteristics decreases the techno-economic significance of renewable energy sources (RES) primarily due to their time-varying energy capacity [17]. For instance, solar PV energy is available during the day, so at night other alternatives or energy storage support are pertinent. Similarly, wind energy systems also impose similar challenges and limitations usually attributed to their unpredictable variability. Such time-varying complexity of RESs makes the integration of energy storage systems (ESS) and dispatchable energy sources pertinent, especially for autonomous RES applications (Figure 1) for various applications, such as appropriate energy mix, ensuring reliability, and reducing operational costs of sustainable energy system [18–20].

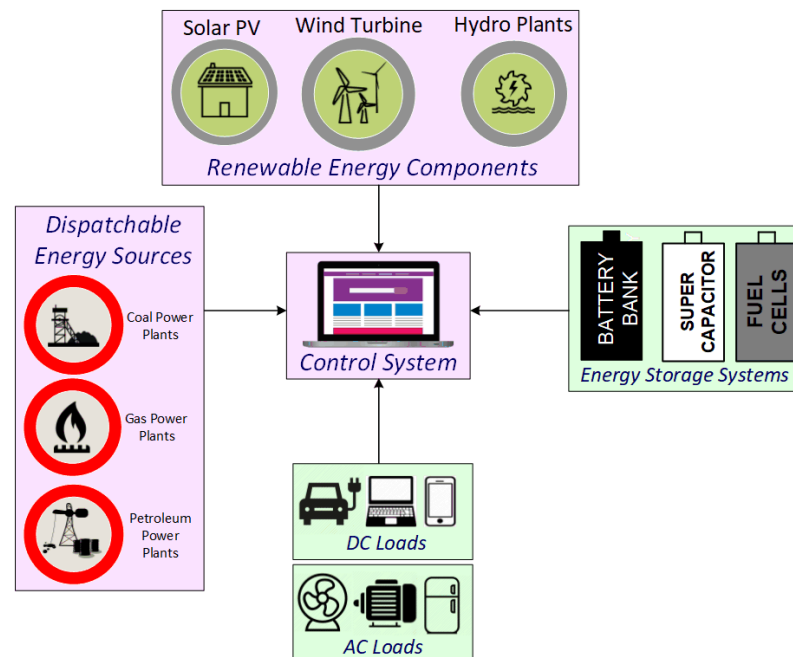


Figure 1. Standalone hybrid energy systems.

The benefits of ESSs are substantial and have long been recognized to be essential towards a coordinated and successful operation of utility grids. Power storage systems mostly include batteries, flywheels, pumped hydro-power storage, supercapacitors, and compressed air energy storage [21]. ESS improves RES integration flexibility through peak-shifting, mitigation of forecasting errors, providing frequency and voltage support among other operational services [22]. Furthermore, expensive grid improvements or outages due to unforeseen demand or any trip-off of any sources connected to the national grid

network can be obviated [23–25]. Accordingly, the meager inertia, voltage, and frequency support introduced due to RES integration can be further facilitated through hybridized ESS [26–28]. In particular, the deteriorating power quality at the distribution level can be obviated through dedicated energy management algorithms to optimally integrate RESs in accordance with the requirements of the energy market, grid standards, and contingencies [29–31].

In this study, a coordinated PSS-SVC is developed to enhance the stability of RES integrated power networks with load sharing device that increases the damping by adding more power system stabilizer value to the system. The main objective of this paper is to enhance the transient stability of renewable integrated power networks. A modified IEEE 9 bus system is considered with solar and wind energy integration incorporated with an appropriate energy storage system that aims to mitigate renewable variability under nominal and light loading conditions. Moreover, a comparative study is also presented between the base case wherein the modified IEEE 9 bus system is incorporated with individual PSS and SVC.

The remainder of the paper is organized as follows. Section 2 presents the related work associated with PSS tuning using different algorithms. Section 3 formulates the equations for stability and load shedding investigation and presents the modeling of the modified IEEE 9 bus under study. Section 4 discusses the results obtained and presents numerous stability studies based on light and nominal loading conditions, and with system fault conditions, followed by the conclusion in Section 5.

## 2. Related Work

Tuning PSS parameters and input signal play an important role in small signal stability investigations of microgrids. The main function of PSS is to produce a torque in phase with the rotor speed deviation and compensate the generator terminal voltage by inserting additional signal [32]. Artificial intelligence (AI) techniques over the last years have been frequently used for PSS tuning. Artificial neural network (ANN) and their types are employed as they can robustly perform based on incomplete data tasks for complex problems while dealing with non-linear problems by easily learning from the historical data. Several network structures have been contemplated for PSS design that includes feed-forward neural networks, recurrent neural network [33], and pole shifting method [34–36].

In the last few years, optimization algorithms have also been developed and proposed to solve PSS designing problems. Tabu search and genetic algorithm (GA) methods are mentioned in [37] for designing PSS. They prove to be more advantageous as the resultant solutions generated are not trapped at the local optimum. Another technique like simulated annealing (SA) is illustrated in [36], for tuning the parameters of PSS. In similar terms, numerous evolutionary and heuristic algorithms have been proposed for parameter tuning of PSS, such as bacteria foraging (BF) process [38] and particle swarm optimization technique (PSO) [39]. A new optimization algorithm that mimics a whale's hunting behavior known as whale optimization algorithm (WOA) is illustrated in [40] in tuning PSS to shift the eigenvalues to a predefined stable zone. Most of the recent power system stability researches investigate new approaches to enhance transient stability effectively and efficiently [41].

However, there are certain limitations to these algorithms. The ANN technique consumes a long training time to choose the number of layers and neurons in each layer and exhaustive training is required [39]. The Pole shifting method imposes a memory storage problem and the computational algorithms are highly complex. The SA method may produce inaccurate results due to being trapped at the local optimum. The GA method may require a long-running time depending on the complexity of the system. The BF algorithm suffers from a delay in reaching the global solution because the algorithm depends on random search directions. PSO has some limitations like partial optimism that affects the speed and direction regulation. Moreover, the algorithm suffers from a weak ability to search locally and that may inadvertently lead to trapping in local minimum

solutions. Although PSS and SVC techniques are mature and prominent, it is also vital to assess their implementation with renewable integration particularly coupled with energy storage systems. An effective operation of PSS and SVC with renewable and energy storage systems can play a significant role in appropriately outlining the potential stability of the system that can be achieved by the system operators. This paper presents quantifiable applicability of the PSS and SVC considering the system dynamics with the integration of renewable energy sources and energy storage systems that is not considered in the literature.

### 3. Problem Formulation and Proposed Framework

#### 3.1. State Space Representation of the Power System Model

In control engineering, a state-space representation is a mathematical model of a physical system as a set of variables of input, output, and state connected by differential equations of the first order. "State space" refers to space whose axes are the state variables. The state of the system can be represented as a vector within that space [42]. A set of  $n$  first-order, nonlinear ordinary differential equations defined in (1) can describe the behavior of a dynamic power system.

$$\dot{x}_1 = f_1(x_1, x_2, \dots, x_n; u_1, u_2, \dots, u_r; t) \quad i = 1, 2, \dots, n \quad (1)$$

where,  $n$  is the order of the system and  $r$  is the number of inputs. This can be written in the following form by using vector-matrix notation as described in (2):

$$\dot{x} = f(x, u, t) \quad (2)$$

The state equations of a power system with  $m$  number of power system stabilizers and  $n$  number of machines can be represented as:

$$\dot{x} = Ax + Bu \quad (3)$$

$$y = Cx + Du \quad (4)$$

$$A = \begin{bmatrix} \frac{\delta f_1}{\delta x_1} & \dots & \frac{\delta f_1}{\delta x_n} \\ \vdots & \ddots & \vdots \\ \frac{\delta f_n}{\delta x_1} & \dots & \frac{\delta f_n}{\delta x_n} \end{bmatrix} \quad B = \begin{bmatrix} \frac{\delta f_1}{\delta u_1} & \dots & \frac{\delta f_1}{\delta u_r} \\ \vdots & \ddots & \vdots \\ \frac{\delta f_n}{\delta u_1} & \dots & \frac{\delta f_n}{\delta u_r} \end{bmatrix} \quad (5)$$

$$C = \begin{bmatrix} \frac{\delta g_1}{\delta x_1} & \dots & \frac{\delta g_1}{\delta x_n} \\ \vdots & \ddots & \vdots \\ \frac{\delta g_m}{\delta x_1} & \dots & \frac{\delta g_m}{\delta x_n} \end{bmatrix} \quad D = \begin{bmatrix} \frac{\delta g_1}{\delta u_1} & \dots & \frac{\delta g_1}{\delta u_r} \\ \vdots & \ddots & \vdots \\ \frac{\delta g_m}{\delta u_1} & \dots & \frac{\delta g_m}{\delta u_r} \end{bmatrix}$$

where,  $A$  is the state matrix of size  $n * n$ ,  $B$  is the input matrix of size  $n * r$ ,  $C$  is the output matrix of size  $m * n$  and  $D$  represents the feedforward matrix of size  $m * r$  (5). The column vector  $u$  is the reference vector to the device. Furthermore, when the state variables derivatives are not explicit time functions, the system is said to be autonomous. In this case, (6) can be simplified to:

$$\dot{x} = f(x, u) \quad (6)$$

Similarly, the output variables (4) that can be observed in the system can be expressed in terms of the state variables and the input variables as:

$$y = g(x, u) \quad (7)$$

Therefore, the complex non-linear power systems and, hence, a set of non-linear differential equations can be defined:

$$x = [\delta, \omega, E'_q, E'_{fd}, V_f] \quad (8)$$

where,  $\delta$  is the rotor angle of the generator,  $\omega$  is the synchronous speed of the generator,  $E'_q$  is the,  $E'_{fd}$  represents the internal voltage of the generator, and  $V_f$  is the excitation voltage of the generator.

### 3.2. PSS Controller Structure

The PSS structure is represented in Figure 2. It consists of a gain constant, a washout filter to serve as a high pass filter, a dynamic compensator to compensate for the phase lag between the electric torque, and the excitation and limiter to prevent the excitation system from entering the saturation mode. The transfer function of the PSS is therefore expressed as:

$$\Delta U_i = k_i \frac{ST_w}{1 + ST_w} \left[ \frac{1 + ST_{1i}}{1 + ST_{2i}} \right] \left[ \frac{1 + ST_{3i}}{1 + ST_{4i}} \right] \Delta \omega_i \quad (9)$$

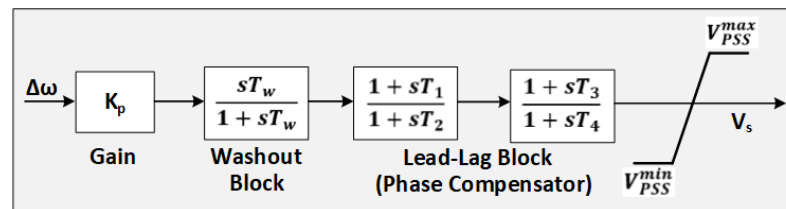


Figure 2. Structure of power system stabilizer.

### 3.3. Operation of IEEE 9 Bus System under Study

An IEEE 9 bus system is considered for this study. It consists of three generators and three loads as depicted in Figure 3. The tests are performed considering a time horizon of 24 h pertaining to its processed data [43]. Table 1 outlines the different loading conditions assessed for the analytical comparative study.

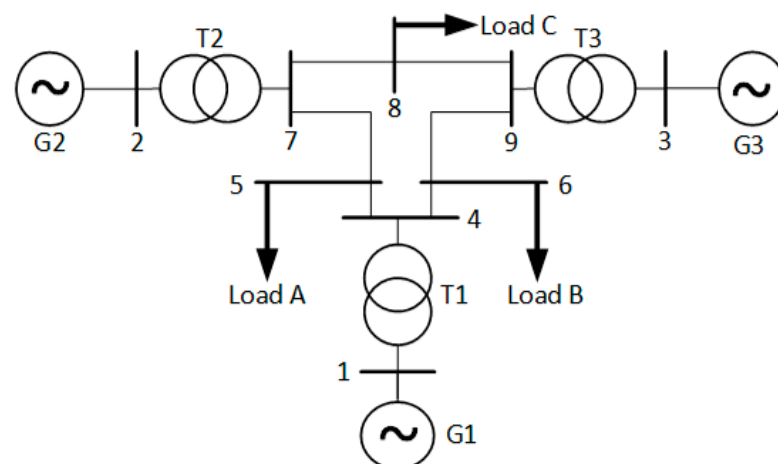


Figure 3. IEEE 9 Bus system without renewable generation.

Further, the load shedding is developed considering two renewable energy sources in the test system (wind turbines and PV cells) under AC power flow taking cost-minimizing as an objective function is illustrated in (10). Correspondingly, the ESS is incorporated in the network to mitigate the RES variability.

$$OF = \sum_{i,t} a_g (P_{i,t}^g)^2 + b_g (P_{i,t}^g) + C_g + \sum_{i,t} VOLL (P_{i,t}^{LS}) + VWC (P_{i,t}^{WVC}) \quad (10)$$

where,  $a_g$ ,  $b_g$ , and  $c_g$  are the fuel cost coefficients of the thermal generation units VOLL is the value of the loss of load (\$/MWh),  $P_{i,t}^g$  is the active power generated by the thermal unit, VMC is the renewable energy sources,  $P_{i,t}^{LS}$  is the active load shedding at time  $t$  from bus  $i$ , and  $P_{i,t}^{WVC}$  denotes the curtailed power from the renewables at time  $t$  from bus  $i$ .

$$-P_{ij}^{max} \leq P_{ij}(t) \leq P_{ij}^{max} \quad (11)$$

$$P_g^{min} \leq P_g(t) \leq P_g^{max} \quad (12)$$

$$P_g(t) - P_g(t-1) \leq RU_g \quad (13)$$

$$-P_g(t-1) - P_g(t) \leq RD_g \quad (14)$$

$$SOC_i(t) = SOC_i(t-1) + (P_i^c(t)\eta_c - P_i^d/\eta_d)\Delta_t \quad (15)$$

$$P_{i,min}^c \leq P_i^c(t) \leq P_{i,max}^c \quad (16)$$

$$P_{i,min}^d \leq P_i^d(t) \leq P_{i,max}^d \quad (17)$$

$$SOC_{i,min} \leq SOC_{i,t} \leq SOC_{i,max} \quad (18)$$

The developed framework is optimized using GAMS to obtain an optimal size and allocation of ESS as presented in Table 2 for mitigating the impact of RES variability, and correspondingly the turn ratios of the distribution transformer are reduced to decrease the output voltage of the transformer. The optimization includes power balance equality constraints [44], transmission line constraint (11), generation constraint (12), the generation ramp up (13), and ramp down constraints (14). Furthermore, the constraints of the energy storage system include the charge/discharge characteristics, charge efficiency ( $\eta_c$ ), discharge efficiency ( $\eta_d$ ), and charge/discharge capability that is limited by their maximum power (15)–(18) [45]. The importance of the load shedding study is to avoid blackout points associated with large cost payment as shown in Figure 4 [46]. Therefore, an assessment is made after each optimization step to see the change in load and determine the value of the voltage corresponding to which the system experiences a brownout.

**Table 1.** Load conditions for the IEEE 9 bus microgrid (p.u.).

Generator	Nominal Loading		Light Loading	
	P	Q	P	Q
G1	1.7164	0.6205	0.9649	0.223
G2	1.630	0.0665	1.00	−0.1933
G3	0.85	−0.1086	0.45	−0.2668
Load	P	Q	P	Q
A	1.25	0.5	0.7	0.35
B	0.9	0.3	0.5	0.3
C	1.0	0.35	0.6	0.2

**Table 2.** Output of GAMS code of optimal size and allocation of ESS for IEEE 9 bus microgrid.

Bus	Optimal Size		Total Size	
	MW	MWh	MW	MWh
5	6.4	12.8	48.3	174.7
6	41.8	161.9	48.3	1744

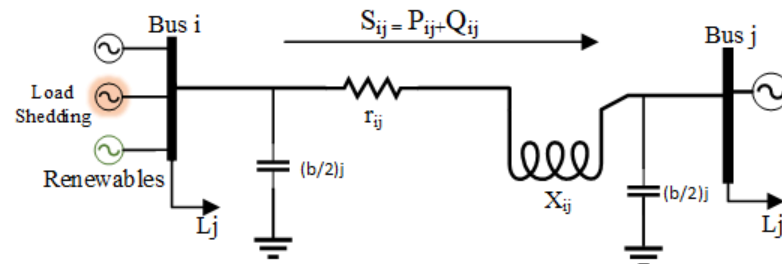


**Figure 4.** Input and output variables of AC power load flow.

3.4. Stabilization Paralleling and Load Sharing between Generators

If two or more generators are connected to a transmission line, assuming the frequency is constant, the models of the generators can be lumped into an equivalent that is powered by the sum of the individual mechanical torque output [47]. The block diagram representation of two parallel-connected generators in synchronous mode (Figure 5) depicts that separate feedback is required for every corresponding loop (here,  $\omega_1$  and  $\omega_2$ ).

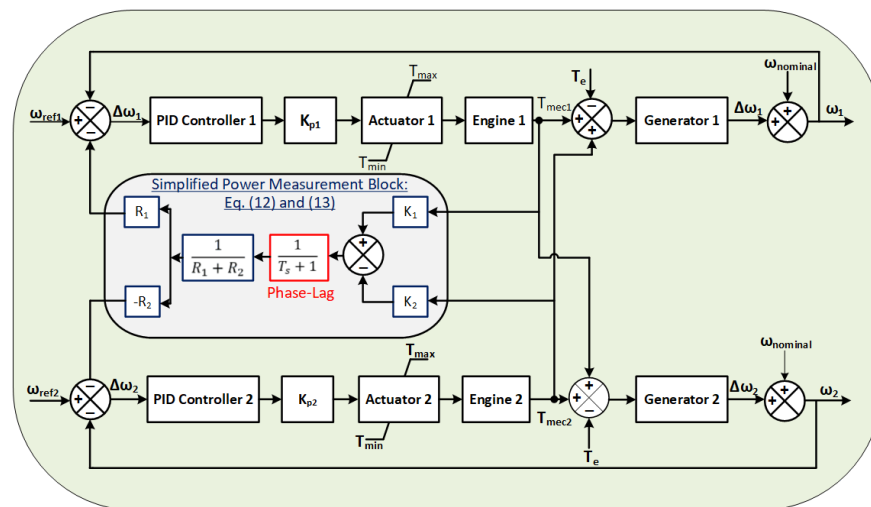


**Figure 5.** Block diagram of two generators connected in parallel in synchronous mode.

Accordingly, the average power of the two system generator sets with load sharing can be represented as an equivalent wattmeter as shown in Figure 6. Therefore, line-to-line voltage, line currents, and battery supply are considered as the inputs to the load sharing unit.

The load-sharing unit output is a DC voltage corresponding to the actual load. All parallel load-sharing units are connected via the parallel cable. To obtain the block diagram of the load sharing circuit, each power measuring circuit is modeled as a voltage source “battery” as shown in Figure 7. Hence, based on the circuit analysis, using Kirchoff’s voltage law, on Figure 7, the voltage source representing the power measuring circuit has a value of the corresponding generator’s electrical power (load) multiplied by a factor ( $k$ ) expressed as:

$$V_1 = K_1 P_{L1}, \quad V_2 = K_1 P_{L1} \tag{19}$$

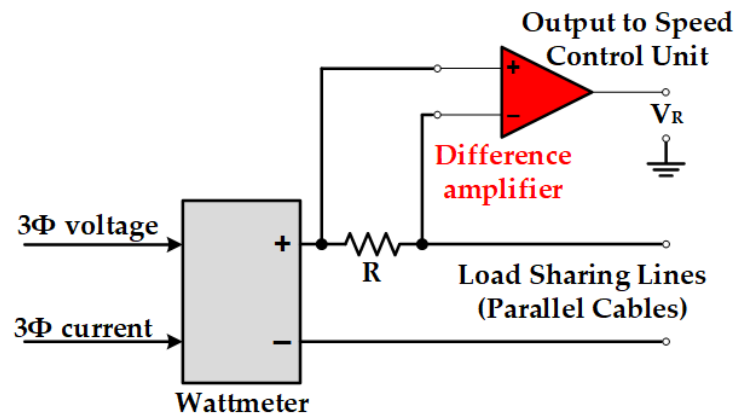


Figure 6. Equivalent load sharing unit.

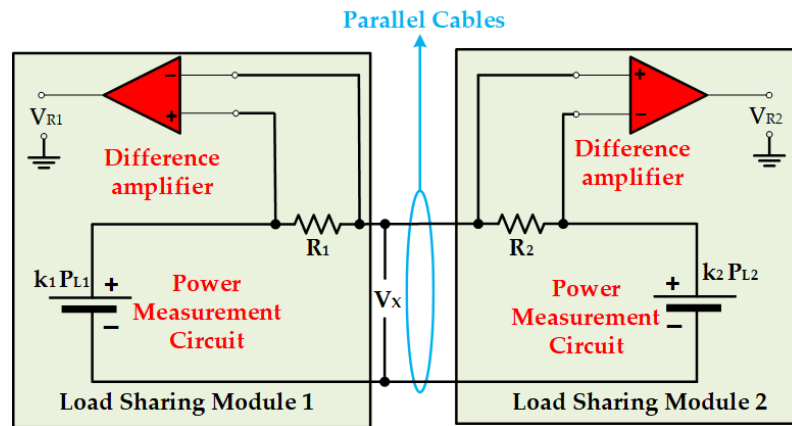


Figure 7. Equivalent load sharing circuit configuration.

The current going through the circuit is:

$$I_{ij,t} = \frac{bV_{i,t}}{2} \angle(\delta_{i,t} + \frac{\pi}{2}) + \frac{V_{i,t} \angle \delta_{i,t} - V_{j,t} \angle \delta_{j,t}}{Z_{ij} \angle \Theta_{ij}} \tag{20}$$

where,  $b$  denotes the line susceptance,  $V_{i,j}$  is the voltage between the bus,  $\delta_{i,j}$  represents the voltage angle,  $Z_{i,j}$  is the line impedance,  $\Theta_{i,j}$  is the phase angle difference between the current and voltage. The output of each difference amplifier (i.e., the voltage across each resistor) (21) and (22). Consequently, based on these formulations the simplified block diagram is developed as depicted in Figure 5. The resultant phase lag system for stabilizing paralleling and load sharing generators are developed and incorporated into the test system under study, that is systematically analyzed to observe the operational performance of the overall system framework and optimization. The apparent power (23) of the system is based on the current flow ( $I_{ij,t}^*$ ) which is the complex conjugate of the current phasor flow between the modules. Accordingly, the active and reactive power flow of between the connecting modules is determined; wherein,  $\theta_{i,j}$  is the angle between the active and reactive power the buses.

$$V_{R1} = I * R_1 = \frac{(K_1 P_{L2} - K_2 P_{L2}) R_1}{R_1 + R_2} \tag{21}$$

$$V_{R2} = -I * R_2 = \frac{-1}{R_1 + R_2} (K_1 P_{L2} - K_2 P_{L2}) R_2 \tag{22}$$

$$S_{ij,t} = (V_{i,t} \angle \delta_{i,t}) I_{ij,t}^* \tag{23}$$

$$P_{ij,t} = \frac{V_{i,t}^2}{Z_{ij}} \cos(\theta_{ij}) - \frac{V_{i,t}V_{j,t}}{Z_{ij}} \cos(\delta_{i,t} - \delta_{j,t} + \theta_{ij}) \quad (24)$$

$$Q_{ij,t} = \frac{V_{i,t}^2}{Z_{ij}} \sin(\theta_{ij}) - \frac{V_{i,t}V_{j,t}}{Z_{ij}} \sin(\delta_{i,t} - \delta_{j,t} + \theta_{ij}) - \frac{bV_{i,t}}{2} \quad (25)$$

#### 4. Results and Discussion

The proposed optimization framework is tested on a modified IEEE 9 bus system (Figure 8). The average inputs values of renewable generation are 92 MW of PV array power at bus 6 and 69 MW of wind power located at bus 5. Furthermore, considering a constant impedance  $z$  corresponding to the varying frequency;  $S = V^2/Z$  and  $S = P + jQ$ . Therefore, the load power is square of the system voltage at constant impedance. Based on this formulation the generator voltage is reduced by 1% in each step, by controlling the power across the load until the generation voltage ratio induces a system brownout and hence marks its critical voltage level. Based on the results obtained (Table 3), it was observed in the lower voltage bound that a system collapse is experienced when the reduction of voltage reached 2% of the nominal voltage of the corresponding bus (brownout voltage).

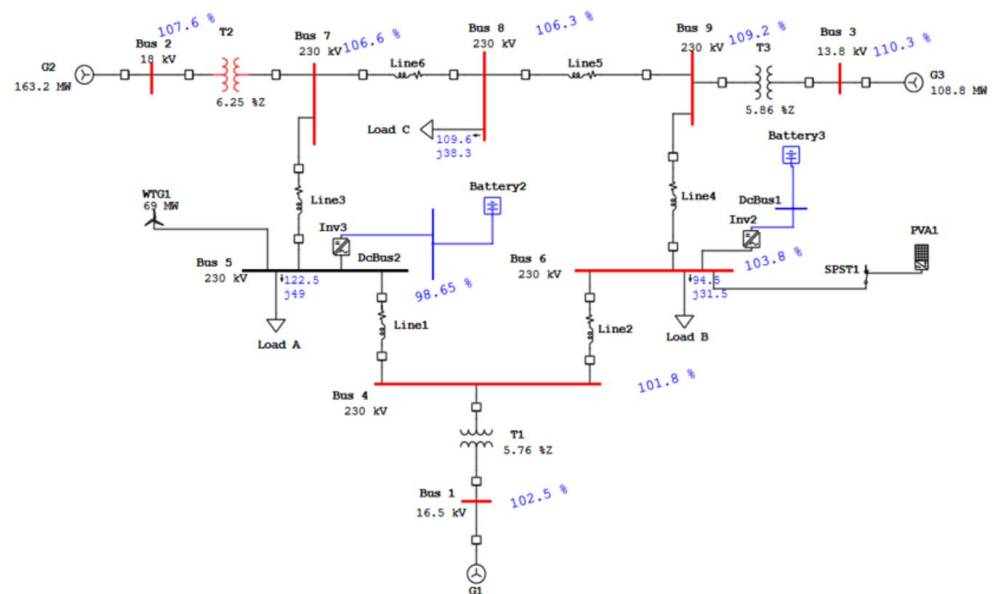


Figure 8. Circuit representation of the modified IEEE 9 bus microgrid under study.

Table 3. Characteristics of load power (MW and MVar) for each voltage ratio.

Voltage Ratio (kV)	Load A		Load B		Load C	
	MW	MVar	MW	MVar	MW	MVar
1	120.874	48.35	87.446	29.149	94.511	33.079
0.99	120.356	48.143	87.072	29.024	92.083	32.929
0.98	119.843	47.937	86.702	28.901	93.658	32.78
0.97	119.333	47.733	86.334	28.778	93.235	32.632
0.96	118.826	47.531	85.969	28.656	92.814	32.485
0.95	118.323	47.329	85.606	28.535	92.396	32.339
0.94	117.824	47.130	85.247	28.416	91.98	32.193
0.93	117.328	46.931	84.89	28.297	91.566	32.048
0.92	116.862	46.745	84.554	28.185	90.975	31.767
0.91	116.372	46.549	84.218	28.067	90.764	31.767
0.90	115.884	46.354	83.851	27.95	90.353	31.624

#### 4.1. Small Signal Stability Analysis

The small signal stability analysis was performed on the integrative combinations of PSS and SVC to the microgrid. The step-wise procedure consists of data acquiring, calculation of matrix  $A$ , along with its eigenvalues ( $\lambda$ ) and participation factor, and applying the PSS/SVC to the system and reassessing the damping of the system. The formal solution of the state equations are obtained by solving for  $\Delta x(s)$  and evaluating  $\Delta y(s)$  (26) and (27). The Laplace transforms of  $\Delta x$  and  $\Delta y$  are seen to have two components, one dependent on the initial conditions and the other on the inputs. These are the Laplace transforms of the free and zero-state components of the state and output vector. The poles of  $\Delta x(s)$  and  $\Delta y(s)$  are the roots of the equation and the values of  $s$  that satisfy the condition (28) are known as the eigenvalues of the matrix  $A$ , whereas (28) denotes the characteristic equation of matrix  $A$ . The eigenvalues (29) are given by the scalar parameters for which there exists a non-trivial solution (i.e.,  $\psi = 0$ ). The eigenvalues are written in the form depicted in (30) and its determinant provides the non-trivial solution. Finally, The  $n$  solutions of  $\lambda = \lambda_1, \lambda_2, \dots, \lambda_n$  are the eigenvalues of  $A$ .

$$\Delta x(s) = (sI - A)^{-1}[\Delta x(0) + B\Delta u(s)] \quad (26)$$

$$\Delta y(s) = C \frac{\text{adj}(sI - A)}{\det(sI - A)} [\Delta x(0) + B\Delta u(s)] + D\Delta u(s) \quad (27)$$

$$\det(sI - A) = 0 \quad (28)$$

$$A\psi = \lambda\psi \quad (29)$$

$$(A - \lambda I)\psi = 0 \quad (30)$$

$$\lambda = \sigma \pm j\omega \quad (31)$$

$$\zeta = \frac{\sigma}{\sqrt{\sigma^2 + \omega^2}} \quad (32)$$

The eigenvalues appear as real or complex conjugate pairs. A real value symbolizes non-oscillatory mode, whereas positive and negative real eigenvalues denote aperiodic monotonic instability and decaying mode, respectively with a greater value symbolizing a faster decay rate. Similarly, every complex conjugate pair represents an oscillatory mode (31). The real ( $\sigma$ ) and imaginary ( $\omega$ ) values of the complex conjugate denote the damping and imaginary component, respectively. A damped oscillation is represented with a negative real value of the complex conjugate, while oscillation with increasing magnitude is denoted by the positive real part [48]. Therefore, the frequency of the oscillation is formulated by,  $f = \frac{\omega}{2\pi}$ . The damping ratio ( $\zeta$ ) is useful in determining the rate at which the amplitude of the oscillation decays (32).

Table 4 displays the nine-bus system frequency and oscillation profiles. The damping ratio for mode 1 and mode 2 are characterized by weak damping, whereas mode 3 and mode 4 are characterized by strong damping. The resultant participation factors are summarized in Table 5. Furthermore, Table 6 displays the participation factor, considering generators having participation factors greater than 4% for weakly damped modes. Pertaining to the synchronous Governing for G1 speed control system as shown in Table 7, the two unstable eigenvalues of the generators (bolded), are recovered based on the pole placement technique and a stable eigenvalues (with negative real parts) are achieved for the generation control system.

Furthermore, unstable eigenvalues are observed during the synchronous mode operation G2 (Table 8), the results depict that the two interacting control systems are struggling

in maintaining their desired speeds. Note that since the saturation effect was not included in the analysis, the values of the mechanical torques will grow without limit. The G2 operation is unstable (bolded poles have positive real parts). This result showed that the two interacting control systems are struggling in maintaining their desired speeds. Note that since the saturation effect was not included in the analysis, the values of the mechanical torques will grow without limit.

**Table 4.** IEEE 9 bus microgrid oscillation profile without the PSS.

Mode	Eigenvalue	Frequency (Hz)	Damping (%)
1	$-0.2945 \pm 11.7009i$	1.86	2.5159
2	$-0.2208 \pm 7.7531i$	1.23	2.8463
3	$-1.0023 \pm 1.9023i$	0.3	46.6145
4	$-1.0775 \pm 0.9651i$	0.15	74.4886

**Table 5.** IEEE 9 bus microgrid participation factors for all the modes.

	Mode 1		Mode 2		Mode 3		Mode 4	
$E'_{g1}$	0.0052	0.0052	0.0263	0.0263	0.4088	0.4088	0.1910	0.1910
$E'_{g2}$	0.0206	0.0206	0.0048	0.0048	0.1535	0.1535	0.4998	0.4998
$E_{fd1}$	0.0004	0.0004	0.0056	0.0056	0.4003	0.4003	0.1865	0.1865
$E_{fd2}$	0.0044	0.0044	0.0016	0.0016	0.1507	0.1507	0.4924	0.4924
$\omega_1$	0.0770	0.0770	0.4201	0.4201	0.0096	0.0096	0.002	0.0023
$\omega_2$	0.4199	0.4199	0.0749	0.0749	0.0047	0.0047	0.0066	0.0066
$\delta_1$	0.0770	0.0770	0.4201	0.4201	0.0096	0.0096	0.0023	0.0023
$\delta_2$	0.4199	0.4199	0.0749	0.0749	0.0047	0.0047	0.0066	0.0066

**Table 6.** Participation factors for weakly damped modes.

	Mode 1		Mode 2	
$\omega_1$	0.0770	0.0770	0.4201	0.4201
$\delta_1$	0.0770	0.0770	0.4201	0.4201
$\omega_2$	0.4199	0.4199	0.0749	0.0749
$\delta_2$	0.4199	0.4199	0.0749	0.0749

**Table 7.** Eigenvalues for G1 speed control system.

Initial Eigenvalues	Eigenvalues after Pole Placement
-111.78	-119.07
-99.26	-90.71
-26.01	-25.19
<b>0.021 + 0.69i</b>	<b>-1.01 + 2.98i</b>
<b>0.02 - 0.69i</b>	<b>-1.02 - 2.98i</b>
-0.14	-0.15

The saturation represents the high and low limits of the fuel valve of the diesel engine. If the saturation is modeled, the valve of the second (decreasing) engine will be fully closed, and the valve opening of the first generator set will settle to a value to produce a mechanical power that matches all the electrical load in the network. This also impacts the operation of G2 under paralleling and load sharing operation as the eigenvalues tend to be unstable. Therefore, based on the developed phase-lag system, stable eigenvalues are generated to reduce the sensitivity of the system under load sharing operation.

For mode 1, the participation factors of the speed and rotor angle of G2 have the largest magnitudes indicating that these states (which are mechanical) have the greatest participation in this mode. For mode 2, the participation factors of the speed and rotor angle of G1 have the largest magnitude. At this point, the mode shape is not known. The mode

shape can be quickly determined from the right eigenvector components corresponding to state variables involved in the mode. Correspondingly, Table 9 shows the right eigenvector components for the weakly damped modes.

**Table 8.** Stability of G2 generation using phase-lag system.

Unstable Synchronous Mode	Unstable Synchronous and Load Sharing Mode	Stability with Phase-Lag System
−98.58	−100.09 + 415.54i	−129.92
112.39	−100.09 − 415.54i	−75.59
−111.12	−129.92	−20.41
−100	−75.59	−113.20
−25.97	−20.41	−97.67
−0.03 + 0.98i	−5.55 + 4.81i	−5.55 + 4.81i
−0.03 − 0.98i	5.55 − 4.81i	−5.55 − 4.81i
−26.04	−32.99	−25.896
$−0.14 \times 10^{-8}$	−0.146	$−2.5 \times 10^{-14}$
<b>3.28 + 2.15i</b>	$−9.81 \times 10^{-15}$	−0.15
<b>3.28 − 2.15i</b>	−0.15	−1.09 + 0.22i
-	-	1.09 − 0.22i

In the case of mode 1, the sign of the real part of the right eigenvector component indicates that G1 swings against G2 yielding an inter-area oscillatory mode. For mode 2, the sign of the real part of right eigenvector components indicates that G1 and G2 swing coherently, yielding another inter-area oscillatory mode. Consequently, PSS is applied to G1 as it has the largest participation in mode 2 as indicated in Table 5. The resultant new system values after PSS insertion are shown in Table 10.

**Table 9.** Right eigenvector components associated with mode 1 and 2.

Mode	Machine Affected/Right Eigenvector
1	G1/0.0002 − 0.0069i      G2/−0.0006 − 0.0257i
2	G1/0.0004 − 0.0155i      G2/0.0005 − 0.0106i

**Table 10.** IEEE 9 bus microgrid oscillation profile with integrated PSS in the microgrid.

Mode	Eigenvalues	Frequency (Hz)	Damping (%)
1	$−5.0135 \pm 17.8121i$	2.83	27.0938
2	$−0.4108 \pm 8.1018i$	1.28	5.0638
3	$−0.9165 \pm 1.9103i$	0.3	43.2572
4	$−1.0356 \pm 1.0097i$	0.16	71.6001
5	−52.8288	0	100
6	−9.0226	0	100
7	−0.2016	0	100

Therefore, the PSS adds some stability to the system by enhancing the poor damping modes observed in Table 4, i.e., for mode 1 from 2.51 to 27.09. Similarly, for mode 2 from 2.84 to 5.06. PSS added new modes to the system having no bad effect on the stability of the system. For comparison purposes, the system eigenvalues with and without the proposed PSS-SVC based controllers when applied individually and through coordinated design for two loading conditions (nominal and light) are determined in Table 11 and Table 12 respectively. The corresponding damping torque coefficient ( $K_d$ ) versus the loading variations are shown in Figure 9. It can be observed that the damping characteristics of PSS outperforms SVC in terms at light loading conditions, whereas the coordinated PSS-SVC design facilitates better overall damping characteristics across the loading conditions highlighting comparatively better system stability. Conclusively, the microgrid damping

is observably improved with effective coordination design with maximum estimated  $K_d = 0.35$  (1/s) compared to 0.05 (1/s) for individual PSS (Figure 9). We observe that the microgrid plant does not help stabilize with individual SVC.

**Table 11.** System eigenvalues for nominal loading.

No Control	PSS	SVC	PSS &SVC
$0.5255 \pm 6.5919i$	$-4.88 \pm 7.36i$	$-4.714 \pm 6i$	$-7.61 \pm 31.2i$
$-0.0795$	$0.550$	$0.6176$	$0.2369$
$10.694 \pm 5.661i$	$-4.77 \pm 7.5i$	$-4.72 \pm 6.2i$	$-21.3625$
$5.6612i$	$7.51i$	$-20.223$	$-1.5361$
-	$-101.03$	$-2.5441$	$-1.4023$
-	$-0.400$	$-0.7052$	$-1.0797$
-	$-0.2$	$-0.2$	$-1.0065$
-	-	-	$-0.5401$
-	-	-	$-0.3733$
-	-	-	$-0.2002$
-	-	-	$-0.2000$

**Table 12.** System eigenvalues for light loading.

No Control	PSS	SVC	PSS &SVC
$0.0382 \pm 0.3601i$	$-1.03 \pm 6.58i$	$-0.66 \pm 6.287i$	$-2.6 \pm 2.8i$
$-0.006$	$0.15$	$0.1047$	$0.6801$
$-10.207 \pm 6.385i$	$-8.96 + -7.08i$	$-9.37 \pm 6.554i$	$-6.91 \pm 16.7i$
-	$7.08i$	$6.5542i$	$-0.69 + -0.08i$
-	$-100.35$	$-20.08$	$-21.2253$
-	$-0.4$	$-1.3933$	$-0.2001$
-	$-0.2$	$-0.7989$	$-0.5226$
-	-	$-0.2$	$-0.3746$
-	-	-	$-0.2$
-	-	-	-

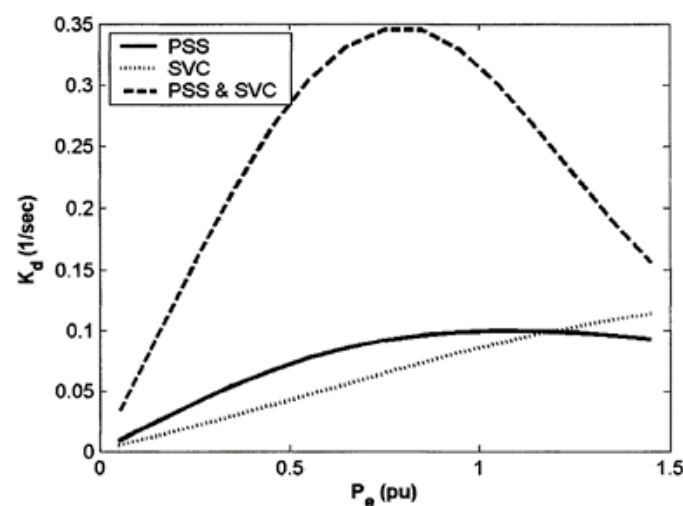


**Figure 9.**  $K_d$  with PSS-SVC based stabilizer.

**4.2. Nonlinear Time-Domain Assessment for Coordinated PSS and SVC Design under System Fault Condition**

To show the optimality and robustness of this coordinated design, the rotor angle ( $\delta$ ), speed deviation ( $\omega$ ), electrical power ( $P_e$ ), and machine terminal voltage responses ( $V_t$ ) are observed through an operational assessment carried out at the nominal and light loading condition specified in Table 1 under a 6-cycle three-phase fault induced in the system. As other generator parameters ( $\Delta\omega, P, V_t$ ) are completely dependent on  $\delta$ , the rotor

angle of G1 connected (slack/swing bus) is used as an objective function under different loading conditions. The simulation results obtained (Figures 10–17) clearly indicate that the proposed coordinated PSS-SVC design outperforms both the individual designs in terms of swing stability, overshoot (in most cases), and settling time.

The 6-cycle fault disturbance was cleared based on the rotor angle response with nominal loading as depicted in Figure 10. The coordinated PSS-SVC design has a smaller settling time which is 4.1 s compared to 5.5 s for individual PSS for reaching a steady state operation. Furthermore, PSS-SVC observably has a better overshoot at almost 1.69 rad as compared to 1.83 rad for individual PSS in dynamic state characteristics. In case of individual SVC, the rotor angle response did not help toward system stabilization and, hence, the 6-cycle fault disturbance was not cleared. In case of light loading conditions, the rotor response was not able to stabilize the system for the individual SVC scenario (Figure 11). On the other hand, the PSS-SVC comparatively experienced a shorter settling time of almost 4 s, in comparison to the 5.3 s setting time experienced with individual PSS design. The overshoot for PSS-SVC incurred at 1.6 rad, in comparison to 1.73 rad for individual PSS in the dynamic state characteristics.

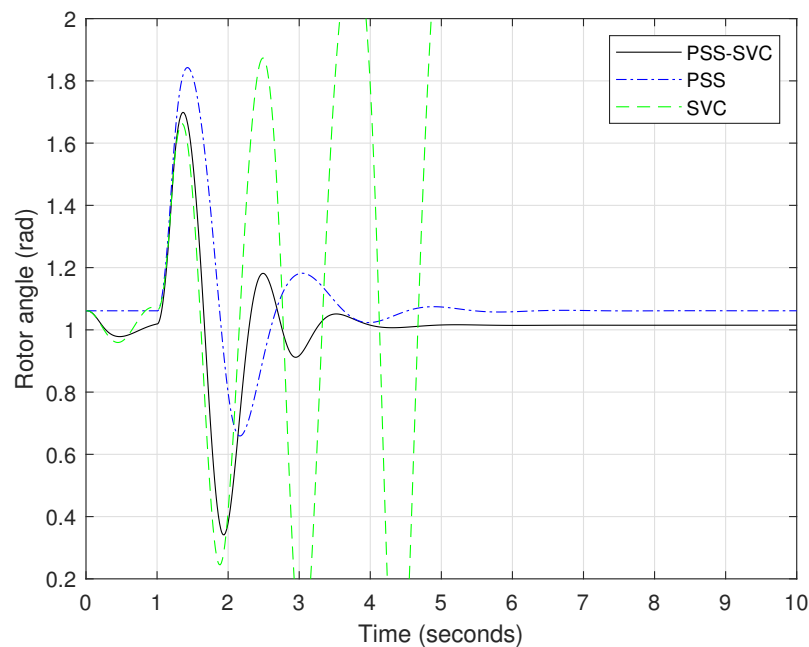


**Figure 10.** Rotor angle response for 6-cycle fault with nominal loading.

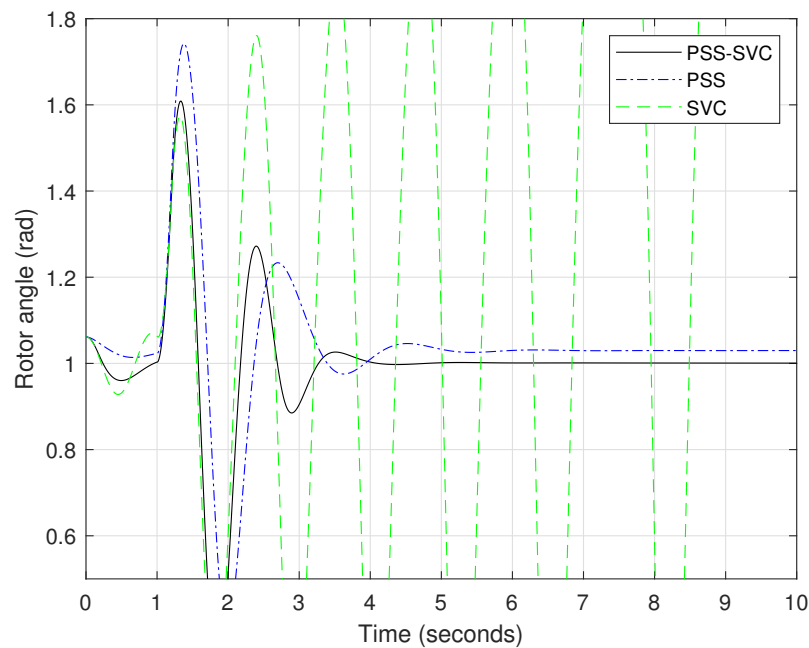


**Figure 11.** Rotor angle response for 6-cycle fault with light loading.

The speed response of the PSS-SVC is able to achieve system stability for nominal as well as light loading conditions. In case of the nominal loading condition (Figure 12), the settling time is observed at 3.6 s and 4.8 s respectively for PSS-SVC and individual PSS designs. The overshoot values observed for both these dynamic design systems are at 1.0 p.u. Accordingly, the settling time observed with PSS-SVC pertaining to speed response in the light loading condition at 3.4 s with overshoot at 1.0 p.u. (Figure 13). On the other hand, with similar overshoot value in case of individual PSS design, the observed settling time to clear the 6-cycle fault disturbance is 5 s. In case of the speed response of the individual SVC design scenario, the fault is not cleared and the system does not attain stability in both the loading scenarios.

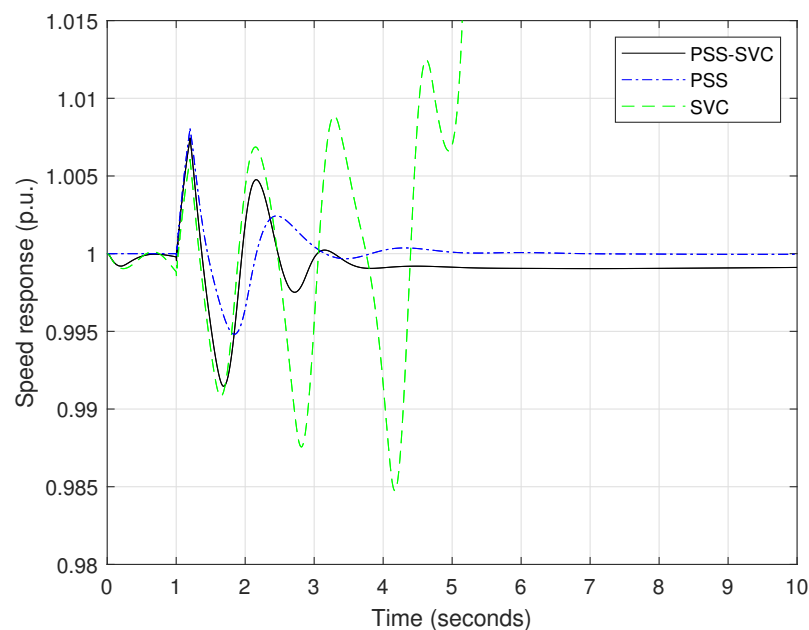


**Figure 12.** Speed response for 6-cycle fault with nominal loading.

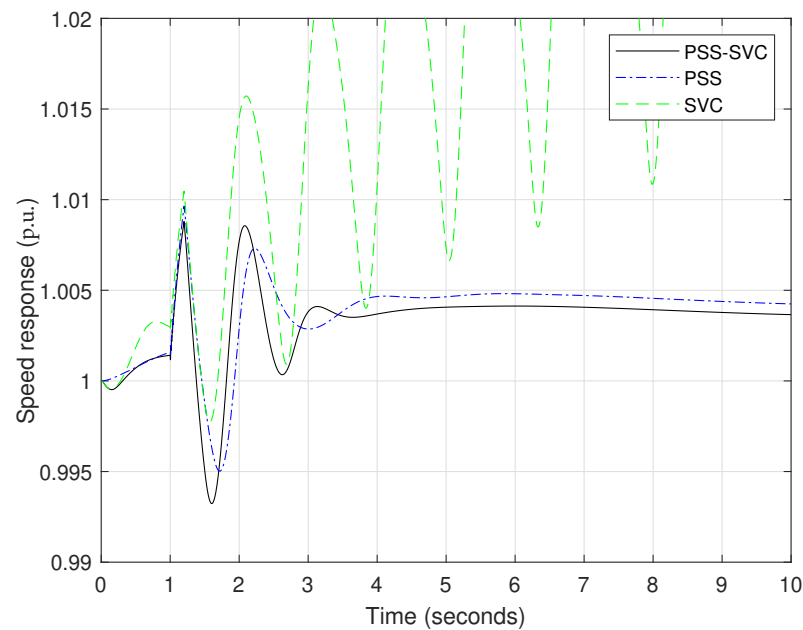


**Figure 13.** Speed response for 6-cycle fault with light loading.

In case of electrical power response, the individual SVC integrative support system response is unable to stabilize the system for both the nominal and light loading scenarios of the IEEE 9 bus system under 6-cycle fault disturbance. A better performance with the PSS-SVC electrical power response system is observed for setting time intervals that are at 4.1 s and 4 s for the nominal and the light loading conditions respectively (Figures 14 and 15). In comparison, the electrical power response of the individual PSS design respectively observes a settling time of 4.2 s and 4.8 s for both the loading scenarios respectively. However, the individual PSS outperforms in case of overshoot with the PSS-SVC incurring a 1.34 p.u. and 1.39 p.u. in comparison to the individual PSS with 1.28 p.u. and 1.31 p.u. overshoot value respectively for the normal and light load system configurations.

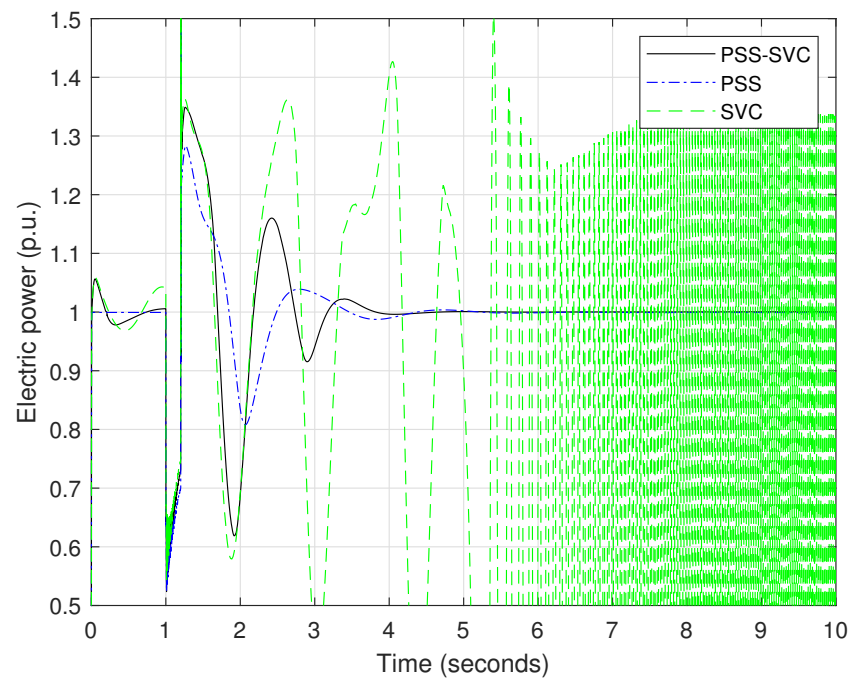


**Figure 14.** Electrical power response for 6-cycle fault with nominal loading.

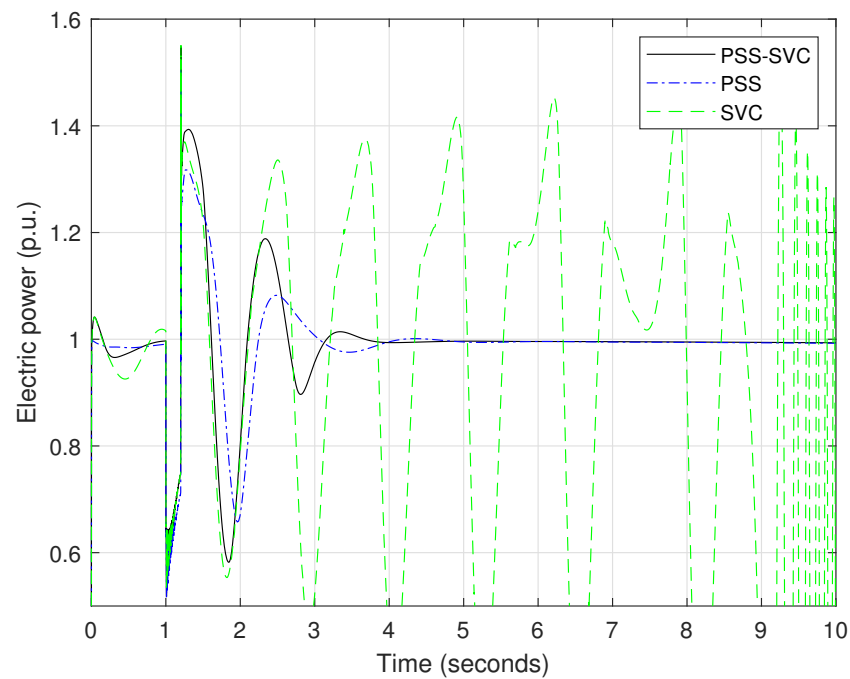


Figure 15. Electrical power response for 6-cycle fault with light loading.

Based on the results obtained pertaining to the terminal voltage as depicted in Figures 16 and 17, the individual PSS and PSS-SVC support response have an overshoot value of 1.22 and 1.04 p.u. during nominal loading, respectively. Accordingly, the terminal voltage response for both PSS-SVC and individual PSS are achieved at similar time interval of 4.2 s. Similarly, in case of light loading conditions of the IEEE 9 bus system, the PSS-SVC voltage response incurred an overshoot value of 1.07 p.u. as compared to the individual PSS terminal voltage response that reaches an overshoot of 1.21 p.u. with both having a settling time of 4.8 s. Furthermore, the individual SVC is observed to have the worst performance and is unable to clear the 6-cycle fault disturbance in both scenarios of the loading conditions.

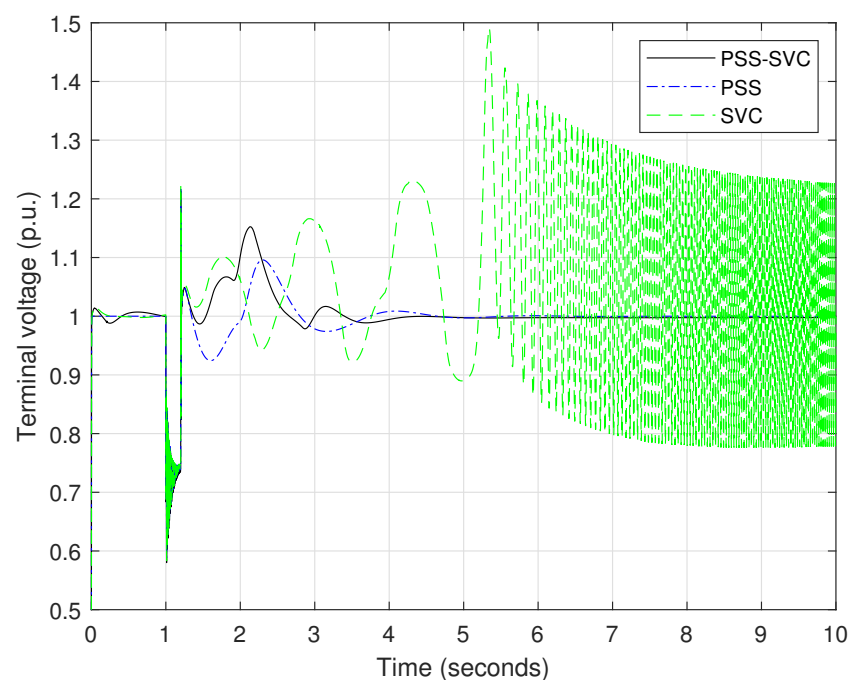
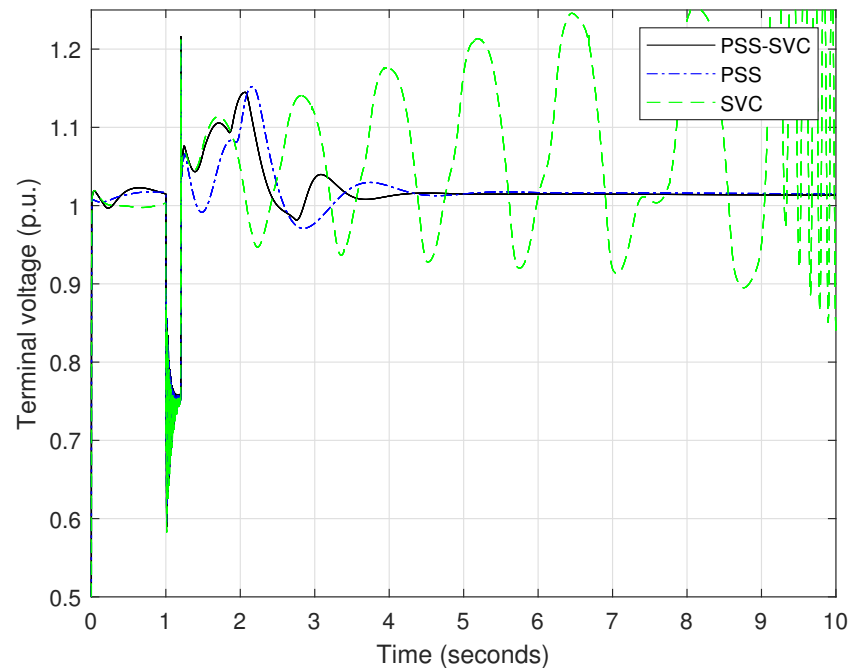


Figure 16. Terminal voltage response for 6-cycle fault with nominal loading.



**Figure 17.** Terminal voltage response for 6-cycle fault with light loading.

Based on the calculated eigenvalues, the coordinated PSS-SVC is postulated to facilitate a better stability of the system with enhanced system responses. Furthermore, these designs are tested and validated on a renewable integrated IEEE 9 bus system with 6-cycle fault condition. During the fault occurrence, rotor angle, speed, electric power, and terminal voltage responses are evaluated for coordinated PSS-SVC, SVC, and PSS. While the coordinated PSS-SVC is observed to have comparatively overall better performance, PSS is observed to facilitate moderately better performance for speed response due to lower overshoot value and similar performance pertaining to the settling time of PSS-SVC for the terminal voltage response of the system.

## 5. Conclusions

This paper presents a coordinated PSS-SVC that was formulated to enhance the stability of hybrid energy system consisting of renewables and energy storage systems. The robustness of the proposed coordinated PSS-SVC design is verified under the most severe disturbance, wherein they facilitate appropriate damping characteristics to the network. The turn ratio of the distribution transformer was reduced to decrease the output voltage of the transformer. The voltage of the three generators was reduced by 1% in each step until blackout was reached and the brownout voltage was determined. The objective is to assess and compare the small signal stability of the IEEE 9 bus system, before and after the insertion of coordinated PSS-SVC design. The simulation results confirm the conclusion drawn for damping torque coefficient analysis that solves the problem of low effectiveness of the individual designs at light loading level. Furthermore, the systems were modeled and analyzed using the state-space method and these systems are two generators connected to a common load, each generator set with synchronous governing, and two generators are connected to a common load, with speed droop (using load sharing module). Therefore, based on an extensive comparative analysis performed with individual SVC and individual PSS, the proposed method improved the network quality in terms of eigenvalues, poles, and voltage profile.

**Author Contributions:** Conceptualization, L.E., K.K., and M.K.; Data curation, K.K. and M.A.-M.; Formal analysis, M.K.; Funding acquisition, M.A.-M. and M.K.; Investigation, L.E., K.K., and M.K.; Methodology, L.E. and M.A.-M.; Project administration, M.A.-M. and M.K.; Resources, M.A.-M. and M.K.; Software, L.E. and K.K.; Supervision, M.A.-M. and M.K.; Validation, L.E., K.K., M.A.-M., and M.K.; Visualization, L.E., M.A.-M. and M.K.; Writing—original draft preparation, L.E. and M.K.; Writing—review and editing, K.K. and M.K. All authors have read and agreed to the published version of the manuscript.

**Funding:** The authors would like to acknowledge the support provided by the Deanship of Research (DSR) at King Fahd University of Petroleum and Minerals (KFUPM) for funding this work through project No. DF191011. In addition, we would like to acknowledge the funding support provided by the King Abdullah City for Atomic and Renewable Energy (K.A. CARE).

**Institutional Review Board Statement:** Not applicable.

**Informed Consent Statement:** Not applicable.

**Data Availability Statement:** Not applicable.

**Acknowledgments:** The authors would like to acknowledge the support provided by the Deanship of Research (DSR) at King Fahd University of Petroleum and Minerals (KFUPM) for funding this work through project No. DF191011. In addition, we would like to acknowledge the funding support provided by the King Abdullah City for Atomic and Renewable Energy (K.A.CARE).

**Conflicts of Interest:** The authors declare no conflict of interest.

## Abbreviations

The following abbreviations are used in this manuscript:

AI	Artificial Intelligence
ANN	Artificial neural network
AVR	Automatic voltage regulator
BF	Bacteria foraging
ESS	Energy storage system
FACTS	Flexible AC transmission system
GA	Genetic algorithm
PSO	Particle swarm optimization
PSS	Power system stabilizer
RES	Renewable energy sources
SA	Simulated annealing
SVC	Static VAR compensator
WOA	Whale optimization algorithm
$\delta$	Rotor angle
$\Delta\omega$	Deviation from the synchronous speed
$V_t$	Terminal voltage of generator
$x$	State variable vector
$u, y$	Input and output vector
$g$	Nonlinear function vector connected to $u, y$
$A$	State matrix
$B$	Input matrix
$C$	Output matrix
$D$	Feedforward matrix
$a_g, b_g, c_g$	Fuel cost coefficients of thermal unit $g$
$OF$	Total operating costs (\$)
$P_{(i,t)}^g$	Active power generated by thermal unit $g$ connected to bus $i$ at time $t$ (MW)

$VOLL$	Value of loss of load (\$/MW h)
$P_{(i,t)}^{LS}$	Active Load shedding in bus $i$ at time $t$ (MW)
$VWC$	Value of loss of wind (\$/MW h)
$P_{(i,t)}^{WC}$	Curtailed power of wind turbine connected to bus $i$ at time $t$ (MW)
$\Delta U_i$	Transfer function of the PSS at bus $i$
$T_w$	Washout time constant
$T_{((1,2,3,4)i)}$	Compensation time constants
$K_d$	Damping torque coefficient

## References

- Lisin, E.; Shuvalova, D.; Volkova, I.; Strielkowski, W. Sustainable development of regional power systems and the consumption of electric energy. *Sustainability* **2018**, *10*, 1111. [\[CrossRef\]](#)
- Mohammed, H. Power system transient stability enhancement by tuning of SSSC and PSS parameters using PSO technique. *J. Univ. Babylon* **2018**, *26*, 81–94. [\[CrossRef\]](#)
- Gbadamosi, S.L.; Nwulu, N.I. Optimal power dispatch and reliability analysis of hybrid CHP-PV-wind systems in farming applications. *Sustainability* **2020**, *12*, 8199. [\[CrossRef\]](#)
- Jethwa, U.K.; Bansal, R.K.; Date, N.; Vaishnav, R. Comprehensive load-shedding system. *IEEE Trans. Ind. Appl.* **2010**, *46*, 740–749. [\[CrossRef\]](#)
- Mansori, M.; Zazi, M. Grid connected photovoltaic energy conversion system modeling and control using SMC-BSC approach. *Int. J. Renew. Energy Res. (IJRER)* **2019**, *9*, 1480–1491.
- Nguyen, T.T.; Mohammadi, F. Optimal placement of TCSC for congestion management and power loss reduction using multi-objective genetic algorithm. *Sustainability* **2020**, *12*, 2813. [\[CrossRef\]](#)
- Schäfer, B.; Yalcin, G.C. Dynamical modeling of cascading failures in the Turkish power grid. *Chaos Interdiscip. J. Nonlinear Sci.* **2019**, *29*, 093134. [\[CrossRef\]](#)
- Dawood, F.; Shafiullah, G.; Anda, M. Stand-alone microgrid with 100% renewable energy: A case study with hybrid solar PV-battery-hydrogen. *Sustainability* **2020**, *12*, 2047. [\[CrossRef\]](#)
- Khan, K.A.; Khalid, M. Hybrid energy storage system for voltage stability in a DC microgrid using a modified control strategy. In Proceedings of the IEEE Innovative Smart Grid Technologies-Asia (ISGT Asia), Chengdu, China, 21–24 May 2019; pp. 2760–2765.
- Gao, K.; Yan, X.; Peng, R.; Xing, L. Economic design of a linear consecutively connected system considering cost and signal loss. *IEEE Trans. Syst. Man Cybern. Syst.* **2019**, *51*, 5116–5128. [\[CrossRef\]](#)
- Nguyen, T.L.; Wang, Y.; Tran, Q.T.; Caire, R.; Xu, Y.; Gavriluta, C. A distributed hierarchical control framework in islanded microgrids and its agent-based design for cyber-physical implementations. *IEEE Trans. Ind. Electron.* **2020**, *68*, 9685–9695. [\[CrossRef\]](#)
- Gao, K.; Wang, T.; Han, C.; Xie, J.; Ma, Y.; Peng, R. A review of optimization of microgrid operation. *Energies* **2021**, *14*, 2842. [\[CrossRef\]](#)
- Khan, K.A.; Khalid, M. A reactive power compensation strategy in radial distribution network with high PV penetration. In Proceedings of the 8th International Conference on Renewable Energy Research and Applications (ICRERA), Brasov, Romania, 3–6 November 2019; pp. 434–438.
- Kerdphol, T.; Rahman, F.S.; Mitani, Y.; Hongesombut, K.; Küfeoğlu, S. Virtual inertia control-based model predictive control for microgrid frequency stabilization considering high renewable energy integration. *Sustainability* **2017**, *9*, 773. [\[CrossRef\]](#)
- Gandoman, F.H.; Ahmadi, A.; Sharaf, A.M.; Siano, P.; Pou, J.; Hredzak, B.; Agelidis, V.G. Review of FACTS technologies and applications for power quality in smart grids with renewable energy systems. *Renew. Sustain. Energy Rev.* **2018**, *82*, 502–514. [\[CrossRef\]](#)
- Yari, S.; Khoshkhou, H. A comprehensive assessment to propose an improved line stability index. *Int. Trans. Electr. Energy Syst.* **2019**, *29*, e2806. [\[CrossRef\]](#)
- Alhumaid, Y.; Khan, K.; Alismail, F.; Khalid, M. Multi-Input nonlinear programming based deterministic optimization framework for evaluating microgrids with optimal renewable-storage energy mix. *Sustainability* **2021**, *13*, 5878. [\[CrossRef\]](#)
- Tu, G.; Li, Y.; Xiang, J. Analysis, control and optimal placement of static synchronous compensator with/without battery energy storage. *Energies* **2019**, *12*, 4715. [\[CrossRef\]](#)
- Movahedi, A.; Niasar, A.H.; Gharehpetian, G.B. LVRT improvement and transient stability enhancement of power systems based on renewable energy resources using the coordination of SSSC and PSSs controllers. *IET Renew. Power Gener.* **2019**, *13*, 1849–1860. [\[CrossRef\]](#)
- Shah, R.; Mithulanathan, N.; Bansal, R. Damping performance analysis of battery energy storage system, ultracapacitor and shunt capacitor with large-scale photovoltaic plants. *Appl. Energy* **2012**, *96*, 235–244. [\[CrossRef\]](#)
- Abo-Khalil, A.G. Grid connection control of DFIG in variable speed wind turbines under turbulent conditions. *Int. J. Renew. Energy Res.* **2019**, *9*, 1260–1271.
- Wu, X.; Shen, X.; Cui, Q. Multi-objective flexible flow shop scheduling problem considering variable processing time due to renewable energy. *Sustainability* **2018**, *10*, 841. [\[CrossRef\]](#)

23. Ghazal, H.M.; Khan, K.A.; Alismail, F.; Khalid, M. Maximizing capacity credit in generation expansion planning for wind power generation and compressed air energy storage system. In Proceedings of the 2021 IEEE PES Innovative Smart Grid Technologies Europe (ISGT Europe), Espoo, Finland, 18–21 October 2021; pp. 1–5.
24. Singh, N.K.; Koley, C.; Gope, S.; Dawn, S.; Ustun, T.S. An economic risk analysis in wind and pumped hydro energy storage integrated power system using meta-heuristic algorithm. *Sustainability* **2021**, *13*, 13542. [[CrossRef](#)]
25. Al-Humaid, Y.M.; Khan, K.A.; Abdulgalil, M.A.; Khalid, M. Two-stage stochastic optimization of sodium-sulfur energy storage technology in hybrid renewable power systems. *IEEE Access* **2021**, *9*, 162962–162972. [[CrossRef](#)]
26. Luo, X.; Wang, J.; Dooner, M.; Clarke, J. Overview of current development in electrical energy storage technologies and the application potential in power system operation. *Appl. Energy* **2015**, *137*, 511–536. [[CrossRef](#)]
27. Akinyele, D.; Rayudu, R. Review of energy storage technologies for sustainable power networks. *Sustain. Energy Technol. Assess.* **2014**, *8*, 74–91. [[CrossRef](#)]
28. Khan, K.A.; Khalid, M. Improving the transient response of hybrid energy storage system for voltage stability in DC microgrids using an autonomous control strategy. *IEEE Access* **2021**, *9*, 10460–10472. [[CrossRef](#)]
29. Huang, H.; Li, F. Sensitivity analysis of load-damping characteristic in power system frequency regulation. *IEEE Trans. Power Syst.* **2012**, *28*, 1324–1335. [[CrossRef](#)]
30. Angalaeswari, S.; Sanjeevikumar, P.; Jamuna, K.; Leonowicz, Z. Hybrid PIPSO-SQP algorithm for real power loss minimization in radial distribution systems with optimal placement of distributed generation. *Sustainability* **2020**, *12*, 5787. [[CrossRef](#)]
31. Koochi-Fayegh, S.; Rosen, M. A review of energy storage types, applications and recent developments. *J. Energy Storage* **2020**, *27*, 101047. [[CrossRef](#)]
32. Machowski, J.; Bialek, J.; Bumby, J.R.; Bumby, J. *Power System Dynamics and Stability*; John Wiley & Sons: Hoboken, NJ, USA, 1997.
33. Kamalasadani, S.; Swann, G.D.; Yousefian, R. A novel system-centric intelligent adaptive control architecture for power system stabilizer based on adaptive neural networks. *IEEE Syst. J.* **2013**, *8*, 1074–1085. [[CrossRef](#)]
34. Georgilakis, P.S.; Hatzigiargyriou, N.D. Unified power flow controllers in smart power systems: Models, methods, and future research. *IET Smart Grid* **2019**, *2*, 2–10. [[CrossRef](#)]
35. Marinescu, B. Residue phase optimization for power oscillations damping control revisited. *Electr. Power Syst. Res.* **2019**, *168*, 200–209. [[CrossRef](#)]
36. Abido, M. Simulated annealing based approach to PSS and FACTS based stabilizer tuning. *Int. J. Electr. Power Energy Syst.* **2000**, *22*, 247–258. [[CrossRef](#)]
37. Majeed, A.; Ahmad, B.; Singh, Y. Power system stability, efficiency and controllability improvement using facts devices. *Int. J. Eng. Sci.* **2019**, *9*, 19590–19596.
38. Panwar, A.; Sharma, G.; Bansal, R.C. Optimal AGC design for a hybrid power system using hybrid bacteria foraging optimization algorithm. *Electr. Power Components Syst.* **2019**, *47*, 955–965. [[CrossRef](#)]
39. Abido, M. Optimal design of power-system stabilizers using particle swarm optimization. *IEEE Trans. Energy Convers.* **2002**, *17*, 406–413. [[CrossRef](#)]
40. Dasu, B.; Sivakumar, M.; Srinivasarao, R. Interconnected multi-machine power system stabilizer design using whale optimization algorithm. *Prot. Control Mod. Power Syst.* **2019**, *4*, 2. [[CrossRef](#)]
41. Elkhidir, L.; Hassan, A.; Khalid, M. SVC-based controller design via ant colony optimization algorithm. In Proceedings of the 8th International Conference on Renewable Energy Research and Applications (ICRERA), Brasov, Romania, 3–6 November 2019; pp. 301–308.
42. Grigsby, L.L. *Power System Stability and Control*; CRC Press: Boca Raton, FL, USA, 2012; Volume 5.
43. Wang, J.; He, Y. Study on model of interruptible load to participate in reserve market. In Proceedings of the 2009 Asia-Pacific Power and Energy Engineering Conference, Wuhan, China, 27–31 March 2009; pp. 1–4.
44. Mohamed, F.A.; Koivo, H.N. Online management genetic algorithms of microgrid for residential application. *Energy Convers. Manag.* **2012**, *64*, 562–568. [[CrossRef](#)]
45. Salman, U.; Khan, K.; Alismail, F.; Khalid, M. Techno-economic assessment and operational planning of wind-battery distributed renewable generation system. *Sustainability* **2021**, *13*, 6776. [[CrossRef](#)]
46. Soroudi, A. *Power System Optimization Modeling in GAMS*; Springer: Cham, Switzerland, 2017; Volume 78.
47. Nayak, N.; Pani, A. A short term forecasting of PV power generation using couple based particle swarm optimization pruned extreme learning machine. *Int. J. Renew. Energy Res.* **2019**, *9*. [[CrossRef](#)]
48. Ogata, K. *Discrete-Time Control Systems*; Prentice-Hall, Inc.: Hoboken, NJ, USA, 1995.